

A New Spectral-Spatial Sub-Pixel Mapping Model for Remotely Sensed Hyperspectral Imagery

Xiong Xu, *Member, IEEE*, Xiaohua Tong[✉], *Senior Member, IEEE*, Antonio Plaza[✉], *Fellow, IEEE*, Jun Li[✉], *Senior Member, IEEE*, Yanfei Zhong[✉], *Senior Member, IEEE*, Huan Xie[✉], *Member, IEEE*, and Liangpei Zhang[✉], *Senior Member, IEEE*

Abstract—In this paper, a new joint spectral–spatial subpixel mapping model is proposed for hyperspectral remotely sensed imagery. Conventional approaches generally use an intermediate step based on the derivation of fractional abundance maps obtained after a spectral unmixing process, and thus the rich spectral information contained in the original hyperspectral data set may not be utilized fully. In this paper, a concept of subpixel abundance map, which calculates the abundance fraction of each subpixel to belong to a given class, was introduced. This allows us to directly connect the original (coarser) hyperspectral image with the final subpixel result. Furthermore, the proposed approach incorporates the spectral information contained in the original hyperspectral imagery and the concept of spatial dependence to generate a final subpixel mapping result. The proposed approach has been experimentally evaluated using both synthetic and real hyperspectral images, and the obtained results demonstrate that the method achieves better results when compared to other seven subpixel mapping methods. The numerical comparisons are based on different indexes such as the overall accuracy and the CPU time. Moreover, the obtained results are statistically significant at 95% confidence.

Index Terms—Hyperspectral imaging, spectral unmixing, subpixel mapping, super-resolution mapping.

I. INTRODUCTION

DUE to the low spatial resolution generally present in hyperspectral cameras (HSCs), microscopic material mixing, and multiple scattering effects, the spectra measured by HSCs are generally mixtures of the spectral signatures of the materials in a scene [1], [2]. Subpixel mapping techniques are commonly used to determine the subpixel spatial attribution of different classes within a mixed pixel, which is a

very challenging problem [3]. By dividing a pixel into subpixels, subpixel mapping algorithms assign a land-cover class to each subpixel, thus generating a finer classification map [4].

In the literature, many efforts have been directed toward the development of subpixel mapping techniques aimed at obtaining a finer classification map from a lower spatial resolution image [5]–[27]. Most of these algorithms attempt to retrieve the finer map from a previously estimated set of abundance maps, which is commonly obtained by using spectral unmixing techniques. Given a synthetic abundance map degraded from a reference classification map, Mertens *et al.* [5] quantified the attraction values of different classes for subpixels in each mixed pixel and attributed each subpixel with a category accordingly. Unlike the noniterative model, Atkinson *et al.* [6] proposed a pixel swapping algorithm (PSA) which swaps categories of two subpixels until the defined spatial dependence attain a maximum value. Different from the two-category-based spatial dependence function in [6], Verhoeve and De Wulf [7] introduced a deterministic solution based on linear programming to measure the spatial dependence of a classification map, and the proposed method also performed efficiently on simulated satellite images. Furthermore, Zhong and Zhang [8] utilized the same objective function and differential evolution to generate a subpixel mapping result. Artificial neural networks, as powerful tools for nonlinear prediction, have also been used for subpixel mapping purposes. Tatem *et al.* [9] trained a Hopfield neural network (HNN) in order to optimize an initial subpixel map used for further iterations, with the purpose of abundance constraint and spatial autocorrelation maximization. A back propagation neural network (BPNN) [10] has also been used to improve subpixel mapping accuracy by constructing the projection between abundance fractions and the subpixel distribution. In addition to synthetic abundance maps, Tatem *et al.* [11] implemented subpixel mapping on the abundance maps generated with spectral unmixing techniques based on an actual case study. Furthermore, Xu *et al.* [12] proposed a multi-agent system-based subpixel mapping method. In this paper, the impact of unmixing-based abundance maps was investigated on the final subpixel mapping results, as compared with the synthetic ones.

For the aforementioned approaches to obtain the finer classification map from a coarser hyperspectral image, a two-step procedure is generally applied [13]. First, an unmixing step produces a set of abundance maps. Then, based on the

Manuscript received August 18, 2015; revised April 25, 2016 and March 12, 2018; accepted May 15, 2018. Date of publication July 12, 2018; date of current version October 25, 2018. This work was supported in part by the National Key Research and Development Program of China under Project 2018YFB0505404 and in part by the National Natural Science Foundation of China under Project 41401398, Project 41325005, Project 41201426, Project 41171352, and Project 41171327. (Corresponding author: Xiaohua Tong.)

X. Xu, X. Tong, and H. Xie are with the College of Surveying and Geo-Informatics, Tongji University, Shanghai 200092, China (e-mail: vxixiong@tongji.edu.cn; xhtong@tongji.edu.cn; huanxie@tongji.edu.cn).

A. Plaza is with the Hyperspectral Computing Laboratory, Department of Technology of Computers and Communications, Escuela Politécnica, University of Extremadura, E-10071 Cáceres, Spain (e-mail: aplaza@unex.es).

J. Li is with the School of Geography and Planning, Sun Yat-sen University, Guangzhou 510275, China.

Y. Zhong and L. Zhang are with the State Key Laboratory of Information Engineering in Surveying, Mapping and Remote Sensing, Wuhan University, Wuhan 430079, China.

Color versions of one or more of the figures in this paper are available online at <http://ieeexplore.ieee.org>.

Digital Object Identifier 10.1109/TGRS.2018.2842748

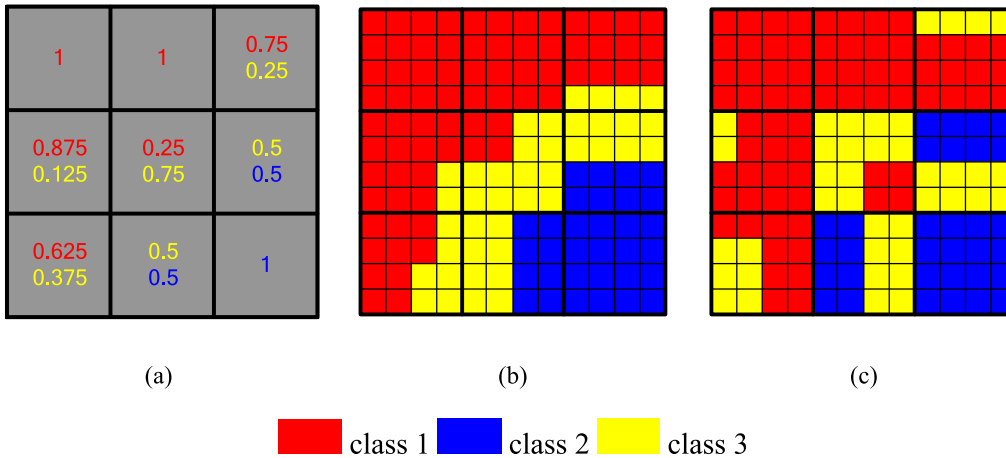


Fig. 1. Toy example illustrating subpixel mapping methods. (a) Abundance maps are extracted for a 3×3 -pixel image. (b) Possible distribution of subpixels in a finer resolution image in which a coarse pixel is divided into $16 (4 \times 4)$ subpixels. (c) Another distribution perceived as less optimal than the one reported in (b).

obtained abundance maps, a subpixel mapping step is used to produce the final result. Therefore, the final subpixel mapping results strongly rely on the unmixing step, which is directly responsible for the quality of the abundance maps. This “unmixing-mapping” procedure represents the main research direction adopted by subpixel mapping techniques in [3]–[27]. On the one hand, better abundance maps exhibit the potential to promote the development of subpixel mapping techniques [28], [29]. However, its drawbacks are also critical. First and foremost, the two steps are performed independently and errors in the first step, such as the unmixing model errors, may propagate to the second one during the process. Another important disadvantage is that the very rich spectral information in the original hyperspectral data set may not be fully exploited for subpixel mapping purposes.

Based on the aforementioned concerns, in this paper, we propose a new joint spectral–spatial subpixel mapping model (SSSM) which directly exploits the original spectral and spatial information contained in the original data set. The spectral information is incorporated via a so-called subpixel abundance map, which indicates the proportions of subpixels to belong to different land-cover classes. As a result, the original hyperspectral image and the final subpixel map can be connected via the subpixel abundance map, without the need for intermediate abundance maps, and the propagation of errors in the model, such as the unmixing model errors, can be mitigated.

The remainder of this paper is organized as follows. Section II outlines the traditional subpixel mapping methods, which exploit a set of abundance maps as their input. Section III provides a detailed description of the proposed SSSM. Section IV explores the performance of the method using both synthetic and real hyperspectral data. Section V concludes this paper with some remarks and hints at plausible future research lines.

II. CONVENTIONAL SUBPIXEL MAPPING METHODS

The key issue in a subpixel mapping problem is how to determine an optimal subpixel distribution of each class

within a pixel. Inspired from Tobler’s [30] first law, spatial dependence refers to the tendency of spatially close observations to be more alike than more distant observations [4]. As illustrated in Fig. 1, given an abundance map obtained by spectral unmixing techniques, each coarse pixel can be divided into $s \times s$ subpixels, where s represents the scale factor. The number of subpixels for each land-cover class can be then determined by the fractional values of different classes. Fig. 1 shows a subpixel mapping example with three classes. As shown in Fig. 1(a), a coarse pixel is divided into $16 (4 \times 4)$ subpixels, where the scale fraction s equals 4, and 0.5 in the fraction image in red, which means that 8 (16×0.5) subpixels belong to land-cover class 1. Fig. 1(b) and (c) describes two possible distributions of subpixels. Given the principle of spatial dependence, the former is perceived to be more optimal.

However, despite the example in Fig. 1, it is difficult to design a specific mathematical model to represent the concept of spatial dependence [31]. As a result, different optimization functions have been employed [5]–[27] using the set of abundance maps as input to the process. Some of typical algorithms used for this purpose are outlined in the following.

A. Attraction Model (AM)

The attraction model (AM) [5] aims at determining the spatial distribution of different classes in mixed pixels by calculating the attraction value of different classes for each subpixel. To quantify the likelihood of a subpixel to be located in the center pixel for different classes, (1) is used to calculate the attraction values for the subpixel and its neighboring pixels

$$p_{a,b}(c) = \text{Avg} \left\{ \frac{P_{i,j}(c)}{d(p_{a,b}, P_{i,j})} \mid P_{i,j} \in N[p_{a,b}] \right\} \quad (1)$$

where $p_{a,b}(c)$ is the attraction value for subpixel $p_{a,b}$ and class c , $P_{i,j}(c)$ is the abundance fraction value for pixel $P_{i,j}$ and class c , $N[p_{a,b}]$ is the neighborhood of the subpixel $p_{a,b}$, s is the scale factor, and $d(p_{a,b}, P_{i,j})$ is the distance between subpixel $p_{a,b}$ and pixel $P_{i,j}$. Attraction values can be calculated for all the subpixels inside a given pixel and, after that, each subpixel will be assigned to a certain class

by sorting the obtained attraction values under the constraints given by the estimated abundance fractions.

B. Pixel Swapping Algorithm (PSA)

As opposed to the AM, which obtains the classification map by comparing the calculated attraction values for each class, an iterative method was utilized by Atkinson [6] in order to achieve an optimal solution by swapping categories of two subpixels. Taking the two-class issue as an example, an initial subpixel mapping result (commonly regarded as 0–1 map) is first obtained. Then, for each subpixel i , its attraction value AV_i is calculated as

$$AV_i = \sum_{j \in N(i)} \lambda_{ij} z(j) \quad (2)$$

where $N(i)$ is the subpixel neighborhood of i , λ_{ij} is the weight of neighboring subpixel j for subpixel i , and $z(j)$ is the value of subpixel j . For all subpixels in a given pixel, two-candidate subpixels will be selected and swapped until the total attraction reaches a maximum value as follows:

$$\begin{aligned} \text{candidate } Q_1 &= (i : AV_i = \max(AV) \| z(i) = 0) \\ \text{candidate } Q_2 &= (j : AV_j = \min(AV) \| z(j) = 1) \end{aligned} \quad (3)$$

C. Genetic Algorithms (GAs)

Genetic algorithms (GAs) [15] have also been introduced for subpixel mapping purposes, in a similar way as the PSA method. For each pixel in the abundance map, an initial population of solutions is generated randomly according to the constraint of abundance fractions of different classes. Each individual of the population is a solution of a possible configuration of different endmembers for a given mixed pixel. Then, different operators such as selection, crossover, and inversion are designed to alter the categories of each subpixel given the following objective function:

$$\text{Fitness} = \sum_{j=1}^{s*s} \sum_{p \in N_s[j]} \frac{\delta_{j,p}}{N_s} \quad (4)$$

where $N_s[j]$ denotes the set of neighboring subpixels of subpixel j , and N_s is the total number of neighboring subpixels. $\delta_{j,p}$ is used here to describe if the neighboring subpixel p b

$$\delta_{j,p} = \begin{cases} 1, & \text{if sub-pixel} \\ p & \text{belongs to the same class with sub-pixel } j \\ 0, & \text{otherwise} \end{cases} \quad (5)$$

Finally, the individual with the best overall fit is identified and retained as the one providing the optimal configuration for a given pixel, after all iterations have been completed.

D. Hopfield Neural Network (HNN)

Tatem *et al.* [9] employ an HNN to accomplish the task of subpixel mapping iteratively. An initial subpixel mapping result should be first obtained. Then, the projection between the input and the output is built as follows:

$$v_{ij}(t) = \frac{1}{2}(1 + \tanh \lambda \mu_{ij}(t)) \quad (6)$$

and the final result can be obtained iteratively as

$$\mu_{ij}(t+1) = \mu_{ij}(t) + \frac{d\mu_{ij}(t)}{dt} dt \quad (7)$$

where $\mu_{ij}(t)$ and $v_{ij}(t)$ denote the input and output of neuron (i, j) , respectively, and λ is a so-called gain parameter. $(d\mu_{ij}(t)/dt)$ indicates the variation of neuron energy, which can be defined as follows:

$$\frac{d\mu_{ij}(t)}{dt} = -\frac{dE}{dv_{ij}}, \quad (8)$$

$$E = -\sum_i \sum_j (k_1 G1_{ij} + k_2 G2_{ij} + k_3 P_{ij}) \quad (9)$$

where $G1_{ij}$, $G2_{ij}$ are indexes of spatial dependence between pixels and subpixels, and P_{ij} is used to indicate the abundance constraint. Furthermore, the three components were defined as follows:

$$\begin{aligned} \frac{dG1_{ij}}{dv_{ij}} &= \frac{1}{2} \left(1 + \tanh \left(\frac{1}{8} \sum_{\substack{k=i-1 \\ k \neq i}}^{i+1} \sum_{\substack{l=j-1 \\ l \neq j}}^{j+1} v_{kl} - 0.5 \right) \lambda \right) \\ &\quad \times (v_{ij} - 1); \\ \frac{dG2_{ij}}{dv_{ij}} &= \frac{1}{2} \left(1 + \left(-\tanh \left(\frac{1}{8} \sum_{\substack{k=i-1 \\ k \neq i}}^{i+1} \sum_{\substack{l=j-1 \\ l \neq j}}^{j+1} v_{kl} \right) \lambda \right) \right) \\ &\quad \times v_{ij}; \\ \frac{dP_{ij}}{dv_{ij}} &= \frac{1}{2S^2} \sum_{k=xS}^{xS+S} \sum_{l=yS}^{yS+S} (1 + \tanh(v_{kl} - 0.55) \lambda) - a_{xy} \end{aligned} \quad (10)$$

where (x, y) is a pixel in the abundance map, a_{xy} is the fraction value of (x, y) , and S is the scale factor. By this way, the optimal HNN subpixel mapping result can be obtained by renewing $\mu_{ij}(t)$ in each iteration.

It is important to note that a soft abundance constraint is used here, which means that the proportions of different classes in the final result may not stay the same as the abundance constraint. In this way, possible errors in the estimated abundance maps can be handled by the HNN.

III. PROPOSED APPROACH

First of all, we define the formulations and notations used when defining our proposed approach. Let $\mathbf{Y} = [\mathbf{y}_1, \dots, \mathbf{y}_n] \in \Re^{b \times n}$ be the observed hyperspectral image with b spectral bands and n pixels, let $\mathbf{M} = [\mathbf{m}_1, \dots, \mathbf{m}_p] \in \Re^{b \times p}$ collect the spectral signatures of p endmembers presented in \mathbf{Y} , and let $\mathbf{A} = [\mathbf{a}_1, \dots, \mathbf{a}_n] \in \Re^{p \times n}$ stand for the abundance maps associated with \mathbf{Y} and \mathbf{M} . Following the linear mixture model, we have:

$$\mathbf{Y} = \mathbf{M}\mathbf{A} + \mathbf{N} \quad \text{s.t.: } \mathbf{A} \geq 0, \quad \mathbf{1}_p^T \mathbf{A} = \mathbf{1}_n^T \quad (11)$$

where $\mathbf{N} \in \Re^{b \times n}$ is the noise in the data, $\mathbf{A} \geq 0$ and $\mathbf{1}_p^T \mathbf{A} = \mathbf{1}_n^T$ are the so-called nonnegative and sum-to-one constraints, and $\mathbf{1}_p^T = [1, 1, \dots, 1]^T$ is a column vector of size p of 1s. It should be noted that as the goal of subpixel mapping is to produce a subpixel classification map, in this

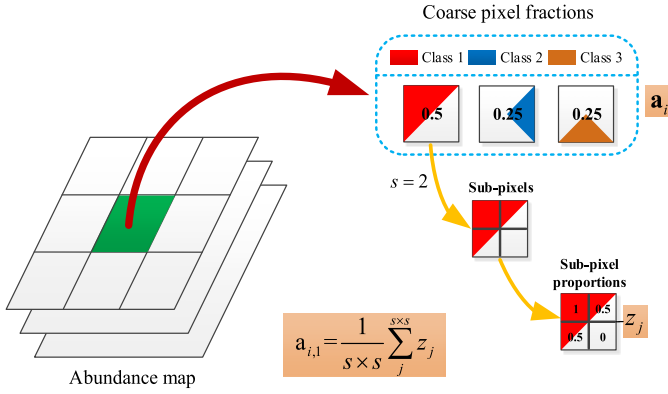


Fig. 2. Toy example illustrating the relationship between a subpixel abundance map and a set of estimated abundance maps.

paper, we assume that the number of endmembers p is the same as the number of classes c , *i.e.*, $p = c$.

Let $\mathbf{Z} = [\mathbf{Z}_1, \dots, \mathbf{Z}_v] \in \mathfrak{R}^{p \times v}$ be the subpixel abundance map, where $v = n \times s^2$ is the number of subpixels in \mathbf{Z} and s is the scaling factor. Obviously, an explicit relationship between the abundance maps and the introduced subpixel abundance map can be easily established by resorting to a downsampling matrix. Fig. 2 illustrates the procedure for constructing the relationship between the abundance maps and the subpixel abundance maps by using a toy example. For a given coarser pixel, the corresponding fractions correspond to three classes (red, blue, and maroon). By taking the red class as an example, we can see that the coarser pixel is divided into 4 subpixels. (The scale factor is 2.) As can be seen in Fig. 2, for each subpixel, we assume a proportion of the belonging class (red), which is different from the traditional assumption that the subpixels are pure and belong to a single unique class. As a result, a linear relationship can be derived as illustrated in Fig. 2.

Similarly, let $\mathbf{D} = [\mathbf{d}_1, \dots, \mathbf{d}_n] \in \mathfrak{R}^{v \times n}$ be the downsampling matrix, which can be constructed as

$$\mathbf{D} = \frac{(\mathbf{I}_l \otimes \mathbf{1}_s^T)^T \otimes (\mathbf{I}_r \otimes \mathbf{1}_s^T)^T}{s^2} \quad (12)$$

where l and r are the number of lines and columns in \mathbf{Y} , respectively, and the total number of samples in the observed image \mathbf{Y} is $n = l \times r$. In (12), \otimes denotes the kronecker operator, \mathbf{I} is an identity matrix with suitable dimension, and s is the scaling factor.

After obtaining the downsampling matrix \mathbf{D} and using the current definitions, we can first build the connection between the abundance map \mathbf{A} and the subpixel abundance map \mathbf{Z}

$$\mathbf{A} = \mathbf{ZD} \quad (13)$$

In Fig. 3, we give a toy example with $n = 4$ pixels in the original image, $v = 16$ pixels in the subpixel abundance map, and the downsampling scale factor $s = 2$, $p = 3$ endmembers (classes). It can be observed that, different from the conventional subpixel mapping approaches, which generally a subpixel map with hard labels of each subpixel, here we obtain the proportions of different classes in each subpixel.

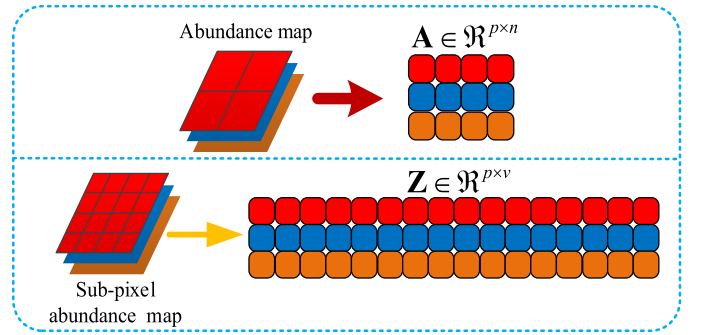


Fig. 3. Graphical illustration of the arrangement of pixels and subpixels in data matrices α and \mathbf{Z} which are arranged in band sequential format [32].

By introducing the downsampling matrix \mathbf{D} and the subpixel abundance map \mathbf{Z} given in (13) into the linear mixture model in (11), we can obtain our proposed subpixel mapping model

$$\mathbf{Y} = \mathbf{MZD} + \mathbf{N} \quad \text{s.t.: } \mathbf{Z} \geq 0, \mathbf{1}_p^T \mathbf{Z} = \mathbf{1}_v^T \quad (14)$$

where $\mathbf{Z} \geq 0$ and $\mathbf{1}_p^T \mathbf{Z} = \mathbf{1}_v^T$, similar to those in (11), are the nonnegative and sum-to-one constraints, respectively. As shown in (14), we can directly associate the final subpixel abundance map \mathbf{Z} with the coarser hyperspectral image \mathbf{Y} , along with the constraints. In the following, we will present how to derive \mathbf{Z} from the proposed subpixel mapping model given in (14).

A. Spatial Prior Constraint

In term of the spatial dependence, a spatial prior constraint can be imposed to regularize the problem. In this paper, we use the anisotropic total variation (TV) model [33] as the spatial prior term. The TV prior can preserve edges and detailed spatial information in the image. It can be represented by

$$\mathbf{TV}(\mathbf{Z}) = |\nabla_x \mathbf{Z}| + |\nabla_y \mathbf{Z}| \quad (15)$$

where ∇_x and ∇_y are linear operators denoting the horizontal and vertical first-order differences. For pixel i of class k in image \mathbf{Z} , its 2-D position can be indicated as (m, q) in which $i = m \times n \times s + q$ and $i \leq v$. Then, each elements in $\nabla_x \mathbf{Z}$ and $\nabla_y \mathbf{Z}$ can be computed as $\nabla Z_{k,i}^x = Z_k[m+1, q] - Z_k[m, q]$ and $\nabla Z_{k,i}^y = Z_k[m, q+1] - Z_k[m, q]$ respectively, where $m = \text{floor}(i/(n \times s))$ and $q = i - m \times n \times s$.

B. Optimization

Finally, the proposed SSSM problem can be generally defined as follows:

$$\min_{\mathbf{Z}} \left\{ |\nabla_x \mathbf{Z}| + |\nabla_y \mathbf{Z}| + \frac{\lambda}{2} \left(\|\mathbf{Y} - \mathbf{MZD}\|_F^2 + \|\mathbf{1}_p^T \mathbf{Z} - \mathbf{1}_v^T\|_2^2 \right) \right\} \quad (16)$$

where $\|\mathbf{Y} - \mathbf{MZD}\|_F^2$ and $\|\mathbf{1}_p^T \mathbf{Z} - \mathbf{1}_v^T\|_2^2$ are data fidelity terms, $|\nabla_x \mathbf{Z}| + |\nabla_y \mathbf{Z}|$ is a regularization term, and λ is a tradeoff parameter. It is hard to solve 1-norm (L_1) regularization problems with methods such as gradient descent. In this paper, a split Bregman method, which is commonly used to solve the L_1 regularization problem by introducing auxiliary variables [34]–[36], is utilized. To apply Bregman splitting,

we first replace $\nabla_x \mathbf{Z}$ by \mathbf{d}_x and $\nabla_y \mathbf{Z}$ by \mathbf{d}_y . This yields the following constrained problem:

$$\begin{aligned} \min_{\mathbf{Z}, \mathbf{d}_x, \mathbf{d}_y} & \left\{ |\mathbf{d}_x| + |\mathbf{d}_y| + \frac{\lambda}{2} \left(\|\mathbf{Y} - \mathbf{M}\mathbf{Z}\mathbf{D}\|_F^2 + \|\mathbf{1}_p^T \mathbf{Z} - \mathbf{1}_v^T\|_2^2 \right) \right\}, \\ \text{s. t. } & \mathbf{d}_x = \nabla_x \mathbf{Z} \quad \text{and} \quad \mathbf{d}_y = \nabla_y \mathbf{Z} \end{aligned} \quad (17)$$

To enforce the constraints on this formulation, (17) is converted to an unconstrained version as follows:

$$\min_{\mathbf{Z}, \mathbf{d}_x, \mathbf{d}_y} \left\{ |\mathbf{d}_x| + |\mathbf{d}_y| + \frac{\lambda}{2} \left(\|\mathbf{Y} - \mathbf{M}\mathbf{Z}\mathbf{D}\|_F^2 + \|\mathbf{1}_p^T \mathbf{Z} - \mathbf{1}_v^T\|_2^2 \right) + \frac{\mu}{2} \left(\|\mathbf{d}_x - \nabla_x \mathbf{Z}\|_F^2 + \|\mathbf{d}_y - \nabla_y \mathbf{Z}\|_F^2 \right) \right\} \quad (18)$$

where μ is the penalty parameter. Finally, the Bregman iteration [34] is applied to enforce the constraints. As a result, we have

$$\min_{\mathbf{Z}, \mathbf{d}_x, \mathbf{d}_y} \left\{ |\mathbf{d}_x| + |\mathbf{d}_y| + \frac{\lambda}{2} \left(\|\mathbf{Y} - \mathbf{M}\mathbf{Z}\mathbf{D}\|_F^2 + \|\mathbf{1}_p^T \mathbf{Z} - \mathbf{1}_v^T\|_2^2 \right) + \frac{\mu}{2} \left(\|\mathbf{d}_x - \nabla_x \mathbf{Z} - \mathbf{b}_x^t\|_F^2 + \|\mathbf{d}_y - \nabla_y \mathbf{Z} - \mathbf{b}_y^t\|_F^2 \right) \right\} \quad (19)$$

where the proper values of \mathbf{b}_x^t and \mathbf{b}_y^t are chosen through the Bregman iteration as follows:

$$\begin{aligned} \mathbf{b}_x^t &= \sum_{j=1}^t (\nabla_x \mathbf{Z}^j - \mathbf{d}_x^j) \\ \mathbf{b}_y^t &= \sum_{j=1}^t (\nabla_y \mathbf{Z}^j - \mathbf{d}_y^j) \end{aligned} \quad (20)$$

To solve the minimization problem in (19), an iterative minimization approach is utilized which solves the following subproblems:

$$\mathbf{Z}^{t+1} = \arg \min \left\{ \begin{aligned} & \frac{\mu}{2} \left(\|\mathbf{d}_x^t - \nabla_x \mathbf{Z} - \mathbf{b}_x^t\|_F^2 + \|\mathbf{d}_y^t - \nabla_y \mathbf{Z} - \mathbf{b}_y^t\|_F^2 \right) \\ & + \frac{\lambda}{2} \left(\|\mathbf{Y} - \mathbf{M}\mathbf{Z}\mathbf{D}\|_F^2 + \|\mathbf{1}_p^T \mathbf{Z} - \mathbf{1}_v^T\|_2^2 \right) \end{aligned} \right\} \quad (21)$$

$$\begin{aligned} \mathbf{d}_x^{t+1} &= \arg \min \left\{ |\mathbf{d}_x| + \frac{\mu}{2} \|\mu \mathbf{d}_x - \nabla_x \mathbf{Z}^{t+1} - \mathbf{b}_x^t\|_F^2 \right\} \\ &= \text{shrink} \left(\nabla_x \mathbf{Z}^{t+1} + \mathbf{b}_x^t, \frac{1}{\mu} \right) \end{aligned} \quad (22)$$

$$\begin{aligned} \mathbf{d}_y^{t+1} &= \arg \min \left\{ |\mathbf{d}_y| + \frac{\mu}{2} \|\mu \mathbf{d}_y - \nabla_y \mathbf{Z}^{t+1} - \mathbf{b}_y^t\|_F^2 \right\} \\ &= \text{shrink} \left(\nabla_y \mathbf{Z}^{t+1} + \mathbf{b}_y^t, \frac{1}{\mu} \right) \end{aligned} \quad (23)$$

$$\mathbf{b}_x^{t+1} = \sum_{j=1}^{t+1} (\nabla_x \mathbf{Z}^j - \mathbf{d}_x^j) = \mathbf{b}_x^t + (\nabla_x \mathbf{Z}^{t+1} - \mathbf{d}_x^{t+1}) \quad (24)$$

$$\mathbf{b}_y^{t+1} = \sum_{j=1}^{t+1} (\nabla_y \mathbf{Z}^j - \mathbf{d}_y^j) = \mathbf{b}_y^t + (\nabla_y \mathbf{Z}^{t+1} - \mathbf{d}_y^{t+1}) \quad (25)$$

where $\text{shrink}(\alpha, \beta) = (\alpha / \|\alpha\|) * \max(\|\alpha\| - \beta, 0)$.

The most commonly used approach to solve subproblem (21) in the literature is the Gauss–Seidel method. However, in our context, (21) cannot be solved by

the Gauss–Seidel method owing to the exact nature of data fidelity terms. The gradient descend method is used instead to minimize the subproblem in (21) as follows:

$$\mathbf{Z}^{t+1} = \mathbf{Z}^t - \rho \nabla E(\mathbf{Z}^t) \quad (26)$$

where $\nabla E(\mathbf{Z}^t)$ is the derivative of the minimization function of (21), and ρ is the step size. Therefore, $\nabla E(\mathbf{Z}^t)$ can be calculated as follows:

$$\begin{aligned} \text{Let } H(\mathbf{Z}^t) &= \nabla \left(\frac{1}{2} \left(\|\mathbf{Y} - \mathbf{M}\mathbf{Z}\mathbf{D}\|_F^2 + \|\mathbf{1}_p^T \mathbf{Z} - \mathbf{1}_v^T\|_2^2 \right) \right) \\ &= \mathbf{M}^T (\mathbf{M}\mathbf{Z}^t \mathbf{D} - \mathbf{Y}) \mathbf{D}^T + \mathbf{1}_p (\mathbf{1}_p^T \mathbf{Z}^t - \mathbf{1}_v^T), \end{aligned}$$

$$\text{Therefore } \nabla E(\mathbf{Z}^t) = \lambda H(\mathbf{Z}^t) - \mu \left[\nabla_x^T (\mathbf{d}_x^t - \mathbf{b}_x^t) + \nabla_y^T (\mathbf{d}_y^t - \mathbf{b}_y^t) + \Delta \mathbf{Z}^t \right] \quad (27)$$

In summary, the split Bregman algorithm can be utilized as indicated in (21)–(25) iteratively until a given number of iterations or a tolerance value of adjacent results is achieved. The split Bregman method is initialized as follows: $\mathbf{d}_x^0 = \mathbf{d}_y^0 = \mathbf{b}_x^0 = \mathbf{b}_y^0 = \mathbf{0}$.

As a result, the subpixel abundance map \mathbf{Z} can be obtained where the value $Z_{k,i}$ in \mathbf{Z} denotes the proportion of pixel i belonging to class k . Then, the subpixel mapping result \mathbf{O} with p classes can be expressed as $\mathbf{O} = f(\mathbf{Z})$, which means that it can be generated with the subpixel abundance map \mathbf{Z} , and different functions $f(\cdot)$ can be used to convert the abundance map to a final subpixel mapping result. In this paper, a simple winner-takes-all strategy was designed to generate the final subpixel mapping result \mathbf{O} as follows:

$$\mathbf{O}_i = j \text{ if } Z_{j,i} = \max\{Z_{k,i} | k \in (1, p)\} \quad (28)$$

IV. EXPERIMENTS AND ANALYSIS

The proposed SSSM has been compared with seven different subpixel mapping algorithms: bilinear interpolation (BI) [17], AM [5], PSA [6], GA [15], HNN [9], BPNN [10], and geometry-based subpixel mapping (GEO) [21]. Among these methods, BI, AM, GA, BPNN, and PSA are based on the exploitation of abundance maps alone, and the number of subpixels of different classes in the mixed pixel is proportional to the obtained abundance fractions. However, the GEO and HNN methods take abundances as soft constraints.

In our experiments, four synthetic and one real hyperspectral images were used to evaluate the proposed SSSM method in comparison to other techniques. For the synthetic image experiments, an original high-resolution hyperspectral image was first degraded to obtain a low-resolution image by applying an averaging filter. The low-resolution image was then used to obtain different subpixel mapping results with spectral unmixing and subpixel mapping techniques. The high-resolution hyperspectral image can be classified to generate a reference classification map to evaluate different subpixel mapping methods. Specifically, a set of test samples were provided for the Pavia center data set and, therefore, they can be used to evaluate the results. For the real experiment, spectral unmixing and subpixel mapping algorithms were applied on the low-resolution hyperspectral image and the classification

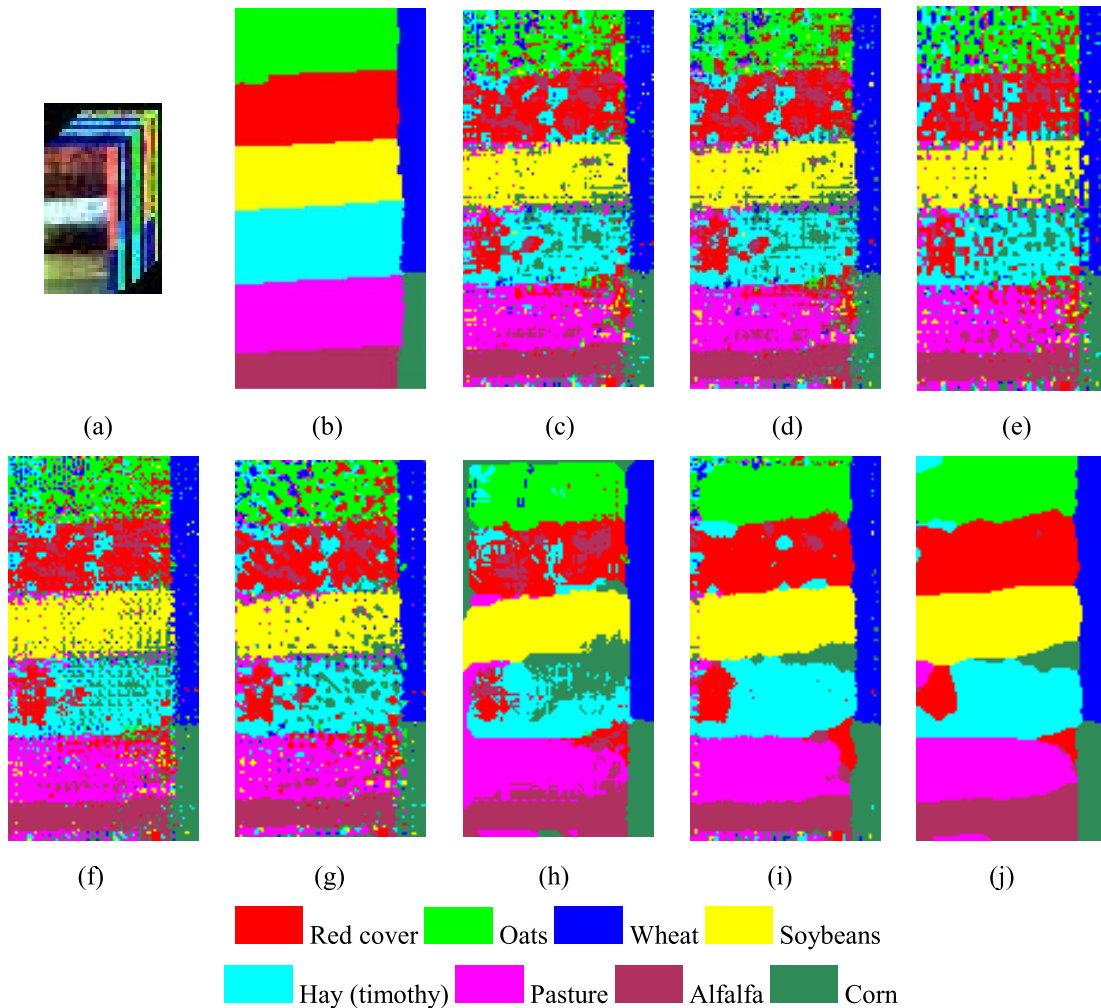


Fig. 4. Subpixel mapping results for the FLC1 data set. (a) Low-resolution image. (b) Reference classification map obtained by eCognition software for the high-resolution image. Subpixel mapping results obtained using (c) BI, (d) AM, (e) GA, (f) BPNN, (g) PSA, (h) GEO, (i) HNN, and (j) SSSM.

result of a high-resolution image which covers an identical area as the low-resolution one was used as the reference map.

For the traditional subpixel mapping methods, the abundance maps were essential and, therefore, a spectral unmixing method should be used first to obtain these abundance fractions. For the proposed method, a subpixel mapping result is utilized as the initial condition and then the final result is obtained after applying the SSSM method iteratively. The fully constrained least-squares method [37] is used to obtain the abundance maps in our experiments. This method naturally satisfies the abundance sum-to-one and nonnegativity constraints.

Our accuracy assessment was undertaken using the overall accuracy (OA), average accuracy (AA), and individual classification accuracy, as well as the Kappa coefficient. Moreover, different parameters were tested for GA (size of population, number of generations, and crossover probability), BPNN (units in the hidden layer, learning rates, and momentum), and HNN (number of iterations, regularization parameter, and step), respectively, and the indexes of OA and Kappa were displayed in the form of mean and standard deviation from 125 results of each method.

Among these results with different parameters for each method, the individual classification accuracy and AA were given for the result that exhibits the best performance.

In addition, to test the statistical significance of differences in accuracy for the results of the proposed method and other algorithms, the McNemar's test [38] is used to compare the misclassification rates with different methods. For the two classification maps C_1 and C_2 , the McNemar's test compares the number of pixels misclassified in C_1 , but not in C_2 (M_{12}), with the number of pixels misclassified in C_2 while not in C_1 (M_{21}). If $M_{12} + M_{21} \geq 20$, X^2 can be considered as a chi-squared distribution (with one degree of freedom) [39], [40] as follows:

$$X^2 = \frac{(|M_{12} - M_{21}| - 1)^2}{M_{12} + M_{21}} \approx \chi_1^2 \quad (29)$$

The McNemar's test accepts the hypothesis that the two classification methods have the same error rate at significance level ε if the value is less than or equal to $\chi_{\varepsilon,1}^2$ [41]. In other words, if the McNemar's value is greater than $\chi_{\varepsilon,1}^2$, the two classification algorithms are significantly different. In this

TABLE I
SUBPIXEL MAPPING ACCURACIES OBTAINED BY DIFFERENT METHODS FOR THE FLC1 DATA SET

Class		Methods							
		BI	AM	GA	BPNN	PSA	GEO	HNN	SSSM
Individual class accuracy (%)	Red Cover	54.69	54.94	54.23	54.89	54.69	59.00	80.49	92.45
	Oats	56.69	56.75	56.17	56.69	56.54	78.37	82.47	87.51
	Wheat	92.49	93.06	88.49	91.84	92.82	95.59	96.57	99.43
	Soybeans	79.45	79.95	76.92	79.51	80.00	86.92	93.90	95.16
	Hay	52.98	53.03	76.92	53.08	53.12	46.74	71.76	71.53
	Pasture	63.73	64.07	63.15	63.97	63.68	68.47	78.40	74.92
	Alfalfa	71.40	71.76	70.25	71.76	71.67	87.74	76.55	92.98
	Corn	90.55	93.11	90.75	94.49	91.14	97.83	98.43	100.00
Average class Accuracy (%)		70.25	70.83	72.11	70.78	70.46	77.58	84.82	89.25
Overall Accuracy (%)		66.19	66.55	65.12 ±0.13	66.27 ±0.22	66.34	72.87	81.47 ±0.52	86.73
Kappa		0.613	0.617	0.601 ±0.002	0.614 ±0.004	0.614	0.690	0.786 ±0.006	0.847
CPU Time(s)		0.1	0.1	38.1	20.1	0.5	1.1	308.2	3.3
McNemar's Test		1971.6	1953.5	2137.0	1916.6	2016.2	1264.5	199.9	

paper, the significance level ε is set as 0.05, which means $\chi_{\varepsilon,1}^2 = 3.841459$.

The remainder of this section is organized as follows. First, we provide an evaluation of the accuracy achieved by the proposed approach (in comparison to other subpixel mapping approaches) using synthetic data. Then, we provide an assessment and comparison using real hyperspectral scenes. This section concludes with an evaluation of the impact of parameter settings on the newly developed SSSM approach.

A. Synthetic Experiments

Four synthetic hyperspectral images are constructed to test the performance of the proposed SSSM method in this experiment. The impact of the point spread function is highly relevant in image downsampling problems [42]. However, in our synthetic experiments, the low-resolution hyperspectral image is generated by simply degrading the available high-resolution image with an averaging filter, and the classification result obtained on the high-resolution image is used as the ground truth to evaluate different subpixel mapping results.

1) *Synthetic-Flightline C1 (FLC1)*: In this section, we use an aerial data set with agricultural crop species and land use, obtained in the 620–660 nm wavelength (band number 12) by an optical mechanical line scanner referred to as the University of Michigan M-7 system. The flightline used in this experiment (called FLC1) was collected on June 28, 1966 [43]. It was taken over the southern part of Tippecanoe County, IN, USA. The size in pixels of the image is 80×160 pixels and the low-resolution image was generated using a resize factor of 4, as shown in Fig. 4(a). Then, a classification result was obtained for FLC1 by classifying the original high-resolution image with the commercial eCognition software. A total of eight land-cover classes can be distinguished in Fig. 4(b). In addition, Fig. 4(c)–(j) shows the subpixel mapping results

obtained using BI, AM, GA, BPNN, PSA, GEO, HNN, and the proposed SSSM, respectively.

A visual comparison of the classification results in Fig. 4 suggests that the proposed SSSM method can obtain the best performance by incorporating the spectral and spatial information of the original low-resolution imagery, particularly when compared to the subpixel mapping results obtained by BI, AM, GA, BPNN, and PSA, whose capacity appear to be limited by a nonoptimal set of abundance maps. This is supported by the fact that the results for these five methods are very similar with regards to each other. Moreover, it is obvious that GEO and HNN generate comparable subpixel mapping results by taking the abundance maps as soft constraints, and spatial information is also utilized to help smooth the results for improved spatial consistency. For example, the results of the latter three methods improve for the Soybeans class by eliminating misclassified pixels.

The subpixel mapping accuracies obtained by different tested methods with the FLC1 data set are listed in Table I. As shown in Table I, the proposed method provided significant improvements in terms of all quantitative indexes when compared with the BI, AM, GA, BPNN, and PSA. Even for the GEO and HNN methods, which give comparable visual results with SSSM, a distinguished quantitative improvement is also observed. This indicates that the proposed SSSM performs competitively when compared to the tested other methods.

Moreover, the CPU time was also reported for each method in Table I. Owing to the fact that methods such as the AM are noniterative, these are the fastest. However, compared with other iterative subpixel mapping methods such as HNN, the proposed method exhibits better performance in terms of accuracy and time consumption. The McNemar's test is a useful tool for determining if two classification methods have significantly different prediction rates. From Table I, it can be

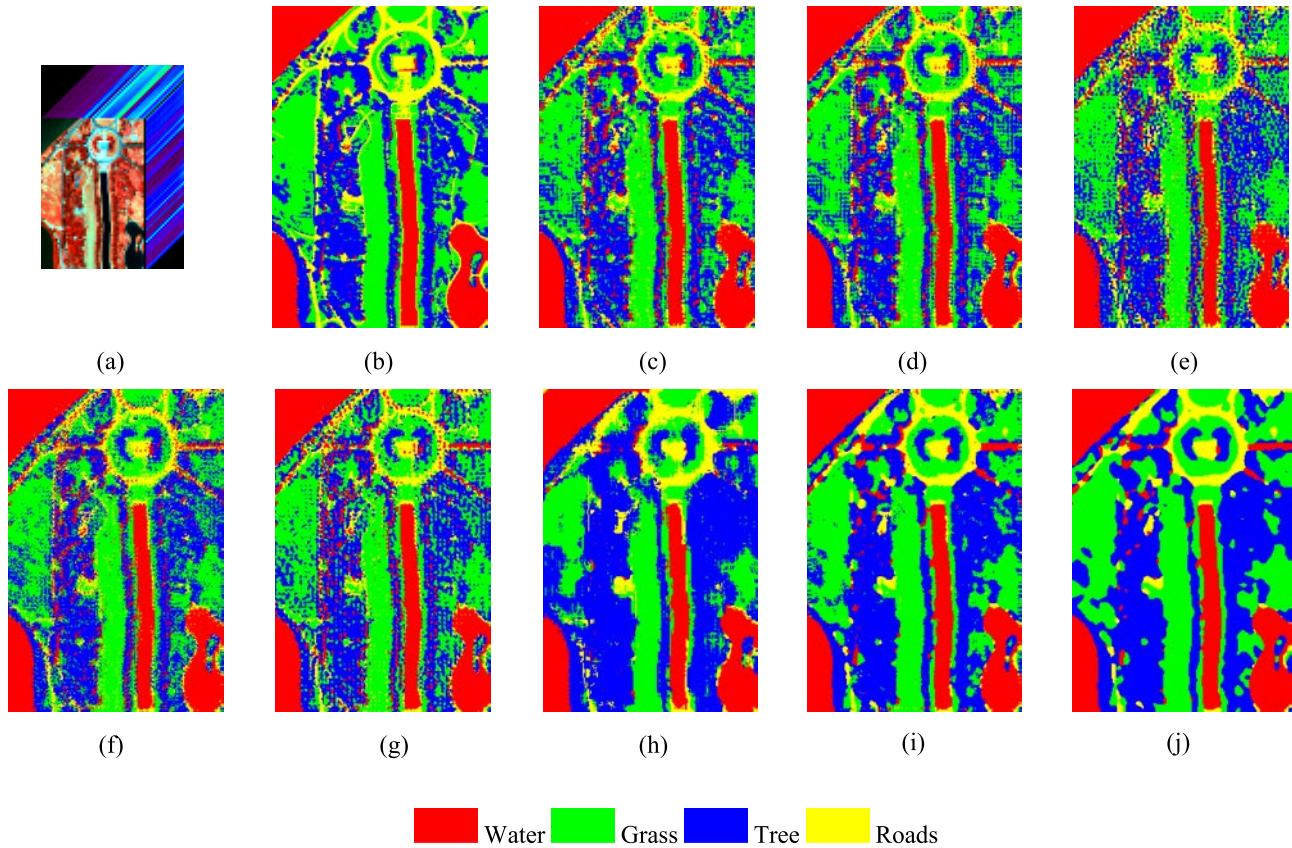


Fig. 5. Subpixel mapping results for the Washington DC data set. (a) Low-resolution hyperspectral imagery. (b) Reference classification map obtained by SVM for the high-resolution imagery. (c) Subpixel mapping result obtained using (c) BI, (d) AM, (e) GA, (f) BPNN, (g) PSA, (h) GEO, (i) HNN, and (j) SSSM.

TABLE II
SUBPIXEL MAPPING ACCURACIES OBTAINED BY THE DIFFERENT TESTED METHODS FOR THE WASHINGTON DC DATA SET

Class		Methods							
		BI	AM	GA	BPNN	PSA	GEO	HNN	SSSM
Individual class accuracy (%)	Water	90.75	91.07	87.46	90.07	90.06	85.98	90.53	90.87
	Grass	75.67	75.93	69.95	74.88	74.12	58.05	79.80	80.26
	Tree	73.67	73.97	69.95	72.76	70.72	87.41	86.88	89.21
	Road	52.08	53.09	44.32	51.36	49.01	48.82	49.33	48.28
Average class Accuracy (%)		73.04	73.52	67.92	72.27	70.98	70.07	76.64	77.16
Overall Accuracy (%)		74.84	75.22	68.90 ±0.13	73.42 ±0.09	72.81	71.39	79.63±0.45	81.05
Kappa		0.646	0.651	0.562 ±0.01	0.634 ±0.002	0.617	0.60	0.711±0.008	0.730
CPU Time (s)		0.1	0.2	167.7	105.3	3.6	1.2	99.7	17.9
McNemar's Test		1224.9	1126.3	3444.8	1416.2	1637.4	3267.4	60.9	

seen that all the values of the McNemar's test are greater than the critical value (3.841459). This implies that the proposed method has significantly different prediction rates compared with other algorithms.

2) *Synthetic-Washington DC HYDICE Image*: The second synthetic image is generated from a part of the Hyperspectral Digital Imagery Collection Experiment airborne hyperspectral data set collected over the Washington DC Mall. A total of 167 bands [44] were used, comprising 300 lines and 200 columns, and the generated low-resolution hyperspectral

image is shown in Fig. 5(a) and (b) shows the reference image classified by the support vector machine (SVM) method, which we use here as the ground truth data. The image comprises four main classes: water, grass, tree, and roads. Fig. 5(c)–(j) illustrates the subpixel mapping results obtained by using BI, AM, GA, BPNN, PSA, GEO, HNN, and the proposed method, respectively.

A visual comparison of the results in Fig. 5 suggests that the proposed method is successful in utilizing the spectral and spatial information on the original hyperspectral image

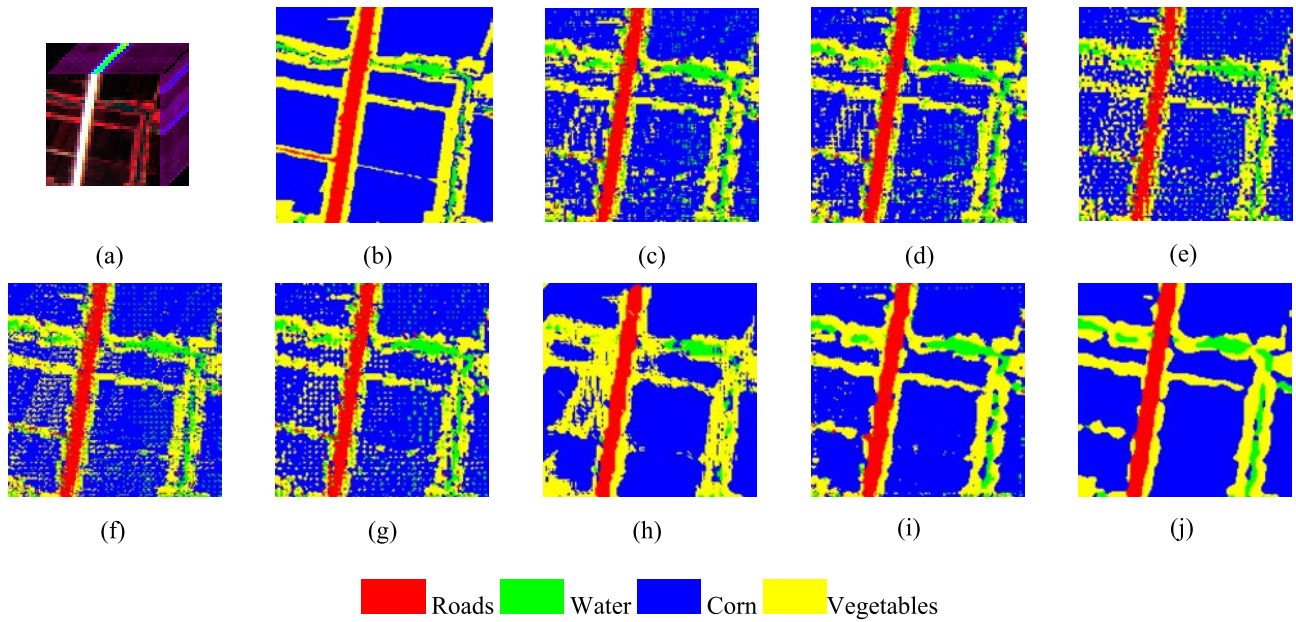


Fig. 6. Subpixel mapping results for the Xiaqiao data set. (a) Low-resolution hyperspectral imagery. (b) Reference classification map obtained by SVM for the high-resolution imagery. Subpixel mapping result obtained using (c) BI, (d) AM, (e) GA, (f) BPNN, (g) PSA, (h) GEO, (i) HNN, and (j) SSSM.

TABLE III
SUBPIXEL MAPPING ACCURACIES OBTAINED BY DIFFERENT TESTED METHODS FOR THE XIAQIAO DATA SET

Class		Methods							
		BI	AM	GA	BPNN	PSA	GEO	HNN	SSSM
Individual class accuracy (%)	Road	79.16	79.75	75.20	80.38	78.85	74.41	86.30	94.13
	Water	58.11	57.97	53.78	59.59	55.00	33.38	61.89	84.86
	Corn	82.75	83.03	82.13	83.25	82.46	83.12	90.76	92.76
	Vegetable	59.19	59.86	55.83	60.79	57.34	69.38	66.25	74.12
Average class Accuracy (%)		69.80	70.15	66.74	71.00	68.41	65.07	76.30	86.47
Overall Accuracy (%)		75.98	76.37	74.16 ±0.14	76.61 ±0.08	75.23	77.66	82.97 ±0.68	88.05
Kappa		0.554	0.561	0.518 ±0.003	0.566 ±0.002	0.540	0.574	0.668 ±0.012	0.766
CPU Time(s)		0.1	0.1	63.2	21.4	0.7	0.1	50.9	6.3
McNemar's Test		2275.1	2218.8	2461.5	1830.0	2349.5	1637.4	662.3	

for subpixel mapping purposes, exhibiting results which are comparable or superior to those obtained by the other tested methods. As compared with the former five subpixel mapping methods, which are exclusively based on the abundance maps, the proposed SSSM achieves a better qualitative appearance of the final subpixel classification maps with smooth borders and spatial consistency. Although the HNN and GEO methods also generate an acceptable result, they provide comparatively lower subpixel classification accuracy.

Table II shows a quantitative comparison of the BI, AM, GA, BPNN, PSA, GEO, HNN, and the proposed SSSM methods. The same conclusions can be drawn as in the experiment with the FLC1 data set. Moreover, the GEO method obtains the second worst result due to the complex distribution of different classes for the Washington DC image. The McNemar's test demonstrates that SSSM gives significantly different results than the other subpixel mapping methods, compared

to the critical value (3.841459). The SSSM can give a better performance by incorporating spectral and spatial information and exhibits the highest subpixel mapping accuracy among all subpixel mapping methods. For the CPU time, similar conclusion can be drawn as for the FLC1 data set.

Synthetic-Xiaqiao PHI Image The third image used in our experiments is a part of a remote sensing image collected with an airborne imaging spectrometer (PHI) from the Xiaqiao test site in China. A total of 80 bands of the PHI image (160 × 160 pixels) were utilized, with a spectral range of 440–854 nm. The scale factor was set as 4, and Fig. 6(a) shows the low-resolution hyperspectral image cube; Fig. 6(b) shows the reference classification map obtained by SVM in which four major land-cover classes can be distinguished: roads, water, corn, and vegetables. Fig. 6(c)–(j) illustrates the subpixel mapping results using BI, AM, GA, BPNN, PSA, GEO, HNN, and SSSM, respectively.

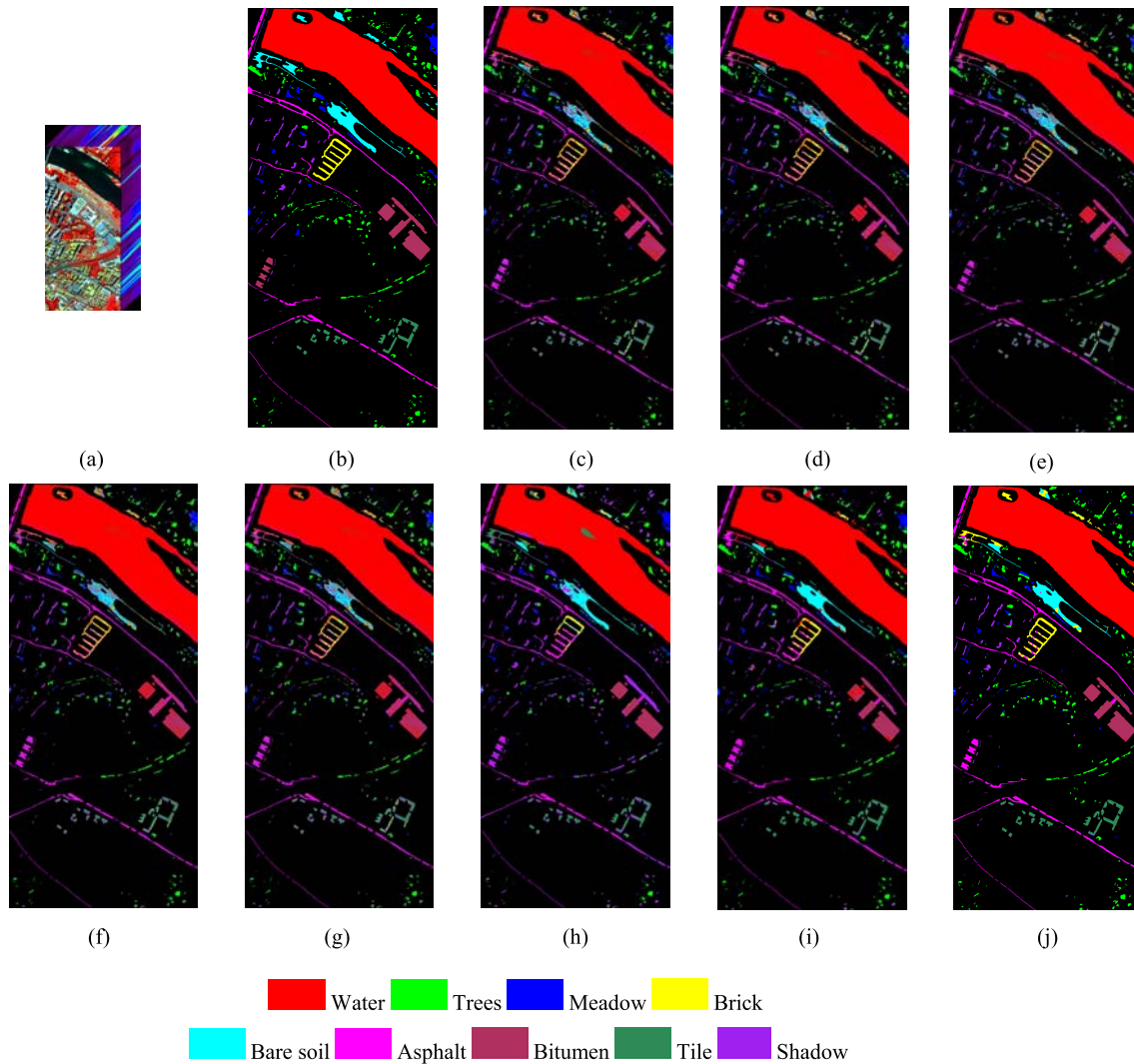


Fig. 7. Subpixel mapping results for the Pavia center data set. (a) Low-resolution hyperspectral imagery. (b) Ground truth samples. Subpixel mapping result obtained using (c) BI, (d) AM, (e) GA, (f) BPNN, (g) PSA, (h) GEO, (i) HNN, and (j) SSSM.

Compared with the reference classification map in Fig. 6(b), additional misclassifications can be observed in the results reported for the traditional subpixel mapping methods. In contrast, GEO, HNN, and the proposed SSSM methods give smoother results in which these noisy pixels are eliminated. By operating on the original low-resolution hyperspectral image directly, the proposed SSSM method can reduce the impact of the considered spectral unmixing technique and achieves good results from a qualitative point of view.

A quantitative assessment for different subpixel mapping methods with the considered data set is shown in Table III, and the proposed method gives the best performance under the considered statistics. Moreover, in this case, the GEO method fails to generate acceptable results. Even for the HNN method, the AA and the OA scores are improved by the proposed method. Again, the comparatively higher accuracies achieved by the proposed SSSM can be attributed to its ability to utilize the spectral and spatial information contained in the original hyperspectral image, thus reducing the error introduced by spectral unmixing in the process. Apparently, both the visual

assessment and quantitative accuracies indicate that SSSM performs better than the other traditional subpixel mapping methods tested in this paper.

3) *Synthetic-Pavia Center Data Set*: Another hyperspectral data set used in this paper was collected in the framework of the HySens project, managed by DLR (the German Aerospace Center), Weßling, Germany, and sponsored by the European Union. This experimental image is a subset of the image of Pavia city center, which was acquired by the Reflective Optics System Imaging Spectrometer (ROSIS) sensor during a flight campaign over Pavia, northern Italy, on July 8, 2002. A total of 97 bands of the ROSIS image (488×1096 pixels) were utilized after some noisy bands were excluded. The scale factor was set as 4. A false-color image consisting of bands 84, 48, and 11 as the R, G, and B bands is illustrated in Fig. 7(a). Fig. 7(b) shows the ground truth to evaluate the classification results. The number of classes in the hyperspectral image was 9: water, tree, meadow, brick, bare soil, asphalt, bitumen, tile, and shadow. Fig. 7(c)–(j) shows the subpixel mapping results using BI, AM, GA, BPNN, PSA, GEO, HNN, and SSSM, respectively.

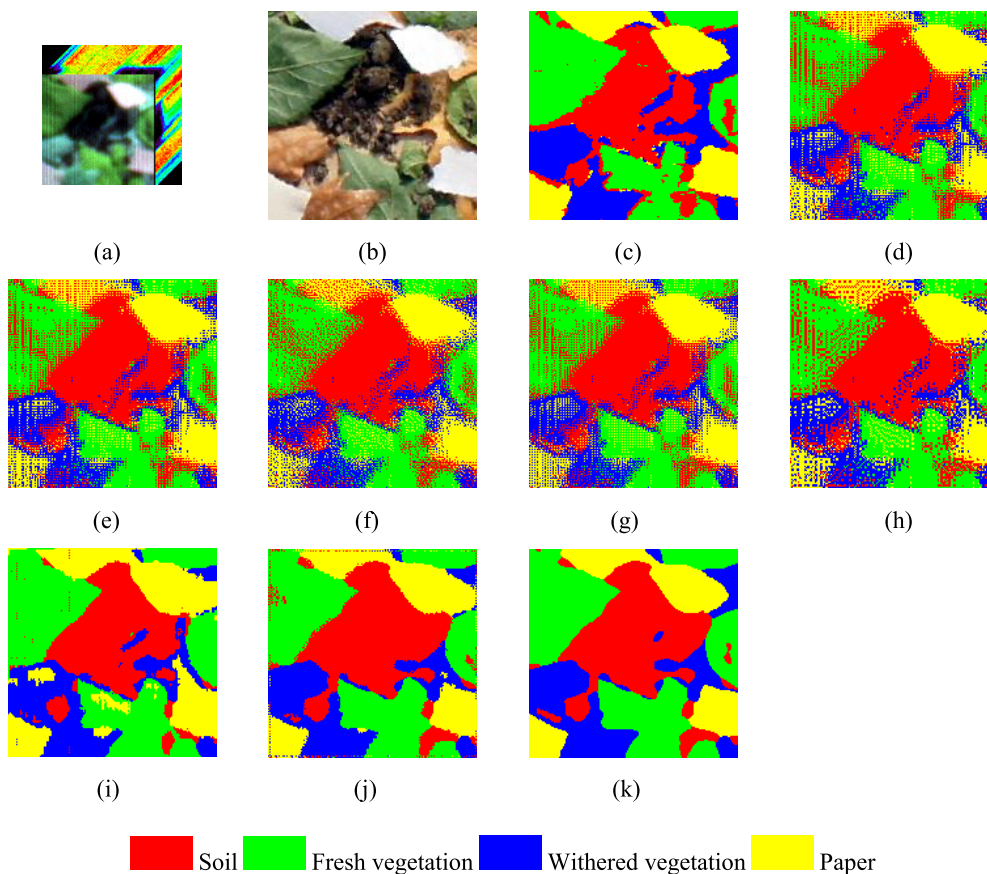


Fig. 8. Subpixel mapping results obtained for the Nuance data set. (a) Low-resolution hyperspectral imagery. (b) High-resolution image obtained with digital camera. (c) Reference classification map obtained by SVM for the high-resolution imagery. Subpixel mapping result obtained using (d) BI, (e) AM, (f) GA, (g) BPNN, (h) PSA, (i) GEO, (j) HNN, and (k) SSSM.

TABLE IV
SUBPIXEL MAPPING ACCURACIES OBTAINED BY DIFFERENT TESTED METHODS FOR THE PAVIA CENTER DATA SET

Class		Methods							
		BI	AM	GA	BPNN	PSA	GEO	HNN	SSSM
Individual class accuracy (%)	Water	98.03	98.04	97.84	97.80	97.82	98.58	99.96	100.00
	Trees	71.99	71.65	64.37	69.07	67.77	42.55	75.21	92.52
	Meadow	61.92	62.58	56.13	59.90	60.10	67.92	72.08	76.86
	Brick	48.93	49.02	42.38	47.76	45.70	32.48	58.69	85.33
	Bare soil	37.98	38.14	38.97	39.18	37.78	58.05	65.58	66.04
	Asphalt	75.35	75.65	70.01	71.66	74.33	53.77	96.37	98.18
	Bitumen	55.35	55.17	53.41	55.26	53.71	65.34	74.50	83.81
	Tile	72.97	73.19	66.59	70.60	69.47	76.01	94.01	96.54
	Shadow	75.70	75.38	72.61	73.16	71.96	91.32	86.84	92.98
Average class Accuracy (%)		66.47	66.54	62.78	64.93	64.29	65.11	80.36	88.03
Overall Accuracy (%)		84.70	84.73	82.76 ±0.09	82.82 ±0.04	83.80	83.86	91.69 ±0.31	94.91
Kappa		0.730	0.731	0.692 ±0.003	0.705 ±0.002	0.714	0.725	0.853 ±0.006	0.912
CPU Time(s)		1.6	2.4	214.2	1263.3	81.0	2.5	2634.2	371.8
McNemar's Test		2275.1	2218.8	2461.5	1830.0	2349.5	1637.4	662.3	

The accuracies and statistics of different methods are listed in Table IV. The best Kappa is obtained by the proposed SSSM with 0.912, compared with the other results which generate

a highest value of 0.853 0.006. Except the difference of accuracies between HNN and SSSM results, the CPU time can also be distinguished apparently. Moreover, the McNemar's

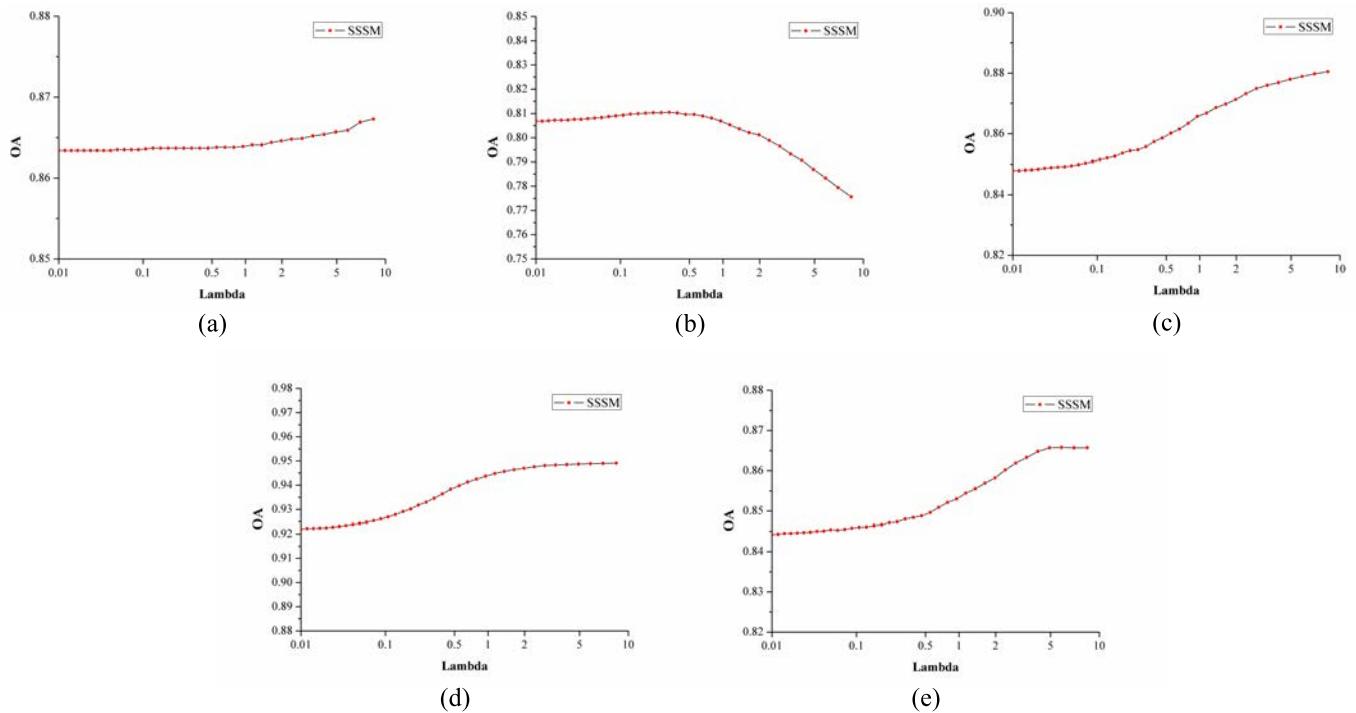


Fig. 9. Comparison of the performance of the proposed method with different parameter settings for all our experiments. (a) Synthetic FLC1 image. (b) Synthetic Washington DC data set. (c) Synthetic Xiaqiao data set. (d) Synthetic Pavia center data set. (e) Real Nuance data set.

TABLE V

SUBPIXEL MAPPING RESULTS OBTAINED BY DIFFERENT METHODS FOR THE NUANCE DATA SET

Class		Methods							
		BI	AM	GA	BPNN	PSA	GEO	HNN	SSSM
Individual class accuracy (%)	Soil	77.24	77.23	75.61	77.16	76.38	76.63	81.05	81.43
	Fresh vegetation	77.51	77.60	76.62	77.44	77.01	92.98	90.83	94.35
	Withered vegetation	60.49	60.51	59.34	77.44	59.81	72.22	71.89	94.35
	Paper	81.70	81.74	79.93	81.57	80.77	95.67	91.92	91.51
Average class Accuracy (%)		74.23	74.27	72.88	78.40	73.49	84.38	83.92	90.41
Overall Accuracy (%)		74.49	74.52	72.08 ±0.65	73.61 ±0.1	73.77	84.20	82.62 ±0.96	86.58
Kappa		0.655	0.655	0.626 ±0.001	0.633 ±0.002	0.645	0.787	0.764 ±0.013	0.818
CPU Time (s)		0.1	0.1	178.2	21.9	0.5	0.2	52.1	6.2
McNemar's Test		2006.5	2002.8	2250.8	1986.2	2116.4	120.7	326.1	

value indicates that SSSM gives a significantly different performance, compared to the other methods, as discussed in this experiment. Overall, the proposed SSSM method generates a better subpixel mapping result by integrating the spectral information in hyperspectral image.

B. Real Experiment-Nuance Data Set

To evaluate the practical application of the proposed method, a real experiment was implemented by acquiring a real hyperspectral image and a higher resolution color image for the same area, simultaneously. The original (low resolution) hyperspectral image (80×80 pixels) was collected

using the Nuance near infrared response imaging spectrometer. The acquired hyperspectral image has 46 bands, and the spectral range is from 650 to 1100 nm, and 10-nm spectral sampling interval. The higher resolution color image (160×160 pixels) was obtained by a digital camera for the same scene, and the considered scale factor was 2. The reference classification map was obtained by classifying the high-resolution color image using the SVM. Four major land-cover classes can be distinguished in this experiment: soil, fresh vegetation, withered vegetation, and white paper. Fig. 8(a)–(c) illustrates the original hyperspectral image, the high-resolution color image, and the high-resolution classification map used

as reference, respectively. Fig. 8(d)–(k) shows the subpixel mapping results obtained using BI, AM, GA, BPNN, PSA, GEO, HNN, and the proposed SSSM approach, respectively.

As opposed to the experiments with synthetic data, additional error sources could be observed in the real-data experiment. The results reported in Fig. 8(d)–(h) are seriously affected by the error of spectral unmixing; the proposed method again provides a smoother subpixel mapping result due to the integration of the spectral and spatial information in the original image. As observed from Fig. 8, the proposed method can provide a better visual result but, however, it can also eliminate some details due to model error and excessive smoothing. As a result, there is a tradeoff between smoothing and detail preservation, in the sense that smoothing can restrain the model error while potentially eliminating small features. Fig. 8 also indicates that GEO and HNN methods generate comparable results as SSSM.

In order to provide a more quantitative evaluation, Table V provides a numerical assessment of different compared methods with the real Nuance hyperspectral data set. The results reported in Table V are similar with regards to those already reported for other methods, with the classic subpixel mapping methods providing comparatively less accurate results than the one reported for the other tested methods. In this experiment, it can also be observed that GEO and HNN can obtain comparable results as SSSM by using the abundances as soft constraints. However, the proposed method still performs better.

C. Parameter Analysis

In the proposed SSSM method, the regularization parameter λ also plays an important role, in the sense that it controls the relative contribution between the data fidelity terms and the spatial prior. To ensure our conclusions can be generalized to data sets with different gray level ranges, all images considered in experiments have been normalized to the range 0–1. We let λ varies from 0.01 to 10 at a rate of 1.2, and Fig. 9 depicts the impact of different values of λ on the obtained accuracy for all considered experiments. Generally, the proposed SSSM is not so sensitive to different regularization parameters; however, some patterns can also be observed. It can be seen that curves for FLC1, Xiaqiao, Pavia center, and Nuance data sets shared similar shape and the optimal results were commonly generated when the parameter is greater than 1. For DC data set, different trends can be found that when higher parameter is given, the accuracy may decrease greatly. Commonly, acceptable results can be generated with the proposed SSSM when the parameter is constrained between 0.5 and 2 for all data sets.

V. CONCLUSION

In this paper, we have presented a new joint SSSM for remotely sensed hyperspectral imagery. The proposed approach incorporates the spectral information of the original image and spatial dependence concepts in order to provide an accurate subpixel mapping result. A main contribution of our method is the introduction of the concept of subpixel abundance map, which establishes the proportions of each subpixel to belong to different land-cover classes. Compared with traditional subpixel mapping methods, which rely strongly on the use of abundance maps for the generation of the

final result, the subpixel abundance map can retain more detailed information about the original spectral information in the hyperspectral image. Our experimental results have been comprehensively conducted using both synthetic and real hyperspectral images, indicating that SSSM is an efficient subpixel mapping technique. The following conclusions can be derived from this paper.

- 1) The utilized subpixel abundance map enables the construction of a linear subpixel mapping model that can be further incorporated into the traditional spectral mixture model, so that the procedure of subpixel mapping can be conducted on the original hyperspectral image directly and provides better results.
- 2) The utilized split Bregman optimization method makes the SSSM method robust and assures the accuracy of the subpixel mapping result given a wide range of values of the regularization parameter λ . Moreover, the impact of point spread function can also be considered in the design of synthetic experiments in future developments, so that a more realistic downsampling process can be further constructed.
- 3) Spectral unmixing and abundance estimation still have a great impact on the proposed method. Although the number of endmembers is assumed to be the same as the number of classes, issues like endmember variability need to be incorporated in future developments of the proposed method with techniques such as sparse representation.
- 4) Since different spatial priors can be easily imposed on the proposed model, in future developments, we are planning on using alternative strategies to model the subpixel information. Moreover, additional experiments can also be carried out to analyze our newly introduced subpixel abundance map, such as to obtain a super-resolution reconstructed version of the original hyperspectral image. Our future work will also focus on the validation of SSSM with different data sets.

Last but not least, we emphasize that the proposed method exhibits significant potential to improve the spatial resolution of available (e.g., HyMAP/AISA/AVIRIS airborne hyperspectral images) and future satellite missions such as EnMAP. This can allow a better exploitation of hyperspectral data in scenarios that require not only high spectral but also high spatial resolution, such as urban monitoring and planning.

ACKNOWLEDGMENT

The authors would like to thank the editor, associate editor, and anonymous reviewers for their helpful comments and suggestions.

REFERENCES

- [1] J. M. Bioucas-Dias *et al.*, “Hyperspectral unmixing overview: Geometrical, statistical, and sparse regression-based approaches,” *IEEE J. Sel. Topics Appl. Earth Observ. Remote Sens.*, vol. 5, no. 2, pp. 354–379, Apr. 2012.
- [2] C.-I. Chang, *Hyperspectral Imaging: Spectral Detection and Classification*. New York, NY, USA: Plenum, 2003.
- [3] P. M. Atkinson, “Issues of uncertainty in super-resolution mapping and the design of an inter-comparison study,” in *Proc. 8th Int. Symp. Spatial Accuracy Assessment Natural Resour. Environ. Sci.*, Shanghai, China, 2004, pp. 145–154.

- [4] P. M. Atkinson, "Mapping sub-pixel boundaries from remotely sensed images," in *Innovations in GIS IV*. London, U.K.: Taylor & Francis, 1997, ch. 12, pp. 166–180.
- [5] K. C. Mertens, B. De Baets, L. P. C. Verbeke, and R. R. De Wulf, "A sub-pixel mapping algorithm based on sub-pixel/pixel spatial attraction models," *Int. J. Remote Sens.*, vol. 27, no. 15, pp. 3293–3310, Sep. 2006.
- [6] P. M. Atkinson, "Sub-pixel target mapping from soft-classified, remotely sensed imagery," *Photogramme. Eng. Remote Sens.*, vol. 71, no. 7, pp. 839–846, 2005.
- [7] J. Verhoeve and R. De Wulf, "Land cover mapping at sub-pixel scales using linear optimization techniques," *Remote Sens. Environ.*, vol. 79, no. 1, pp. 96–104, 2002.
- [8] Y. Zhong and L. Zhang, "Remote sensing image subpixel mapping based on adaptive differential evolution," *IEEE Trans. Syst., Man, Cybern. B. Cybern.*, vol. 42, no. 5, pp. 1306–1329, Oct. 2012.
- [9] A. J. Tatem, H. G. Lewis, P. M. Atkinson, and M. S. Nixon, "Super-resolution target identification from remotely sensed images using a Hopfield neural network," *IEEE Trans. Geosci. Remote Sens.*, vol. 39, no. 4, pp. 781–796, Apr. 2001.
- [10] K. C. Mertens, L. P. C. Verbeke, and R. R. De Wulf, "Sub-pixel mapping with neural networks: Real-world spatial configurations learned from artificial shapes," in *Proc. 4th Int. Symp. Remote Sens.*, Jun. 2003, pp. 1–5.
- [11] A. J. Tatem, H. G. Lewis, P. M. Atkinson, and M. S. Nixon, "Increasing the spatial resolution of agricultural land cover maps using a Hopfield neural network," *Int. J. Geograph. Inf. Sci.*, vol. 17, no. 7, pp. 647–672, Oct./Nov. 2003.
- [12] X. Xu, Y. Zhong, and L. Zhang, "Adaptive subpixel mapping based on a multiagent system for remote-sensing imagery," *IEEE Trans. Geosci. Remote Sens.*, vol. 52, no. 2, pp. 787–804, Feb. 2014.
- [13] X. Xu, "Sub-pixel mapping theory considering spatial characteristic for remote sensing imagery," Ph.D. dissertation, LIESMARS, Wuhan Univ., Wuhan, China, 2013.
- [14] T. Kasetkasema, M. K. Arora, and P. K. Varshney, "Super-resolution land cover mapping using a Markov random field based approach," *Remote Sens. Environ.*, vol. 96, pp. 302–314, Jun. 2005.
- [15] K. C. Mertens, L. P. C. Verbeke, E. I. Ducheyne, and R. R. De Wulf, "Using genetic algorithms in sub-pixel mapping," *Int. J. Remote Sens.*, vol. 24, no. 21, pp. 4241–4247, 2003.
- [16] M. W. Thornton, P. M. Atkinson, and D. A. Holland, "A linearised pixel-swapping method for mapping rural land cover features from fine spatial resolution remotely sensed imagery," *Comput. Geosci.*, vol. 33, no. 10, pp. 1261–1272, Oct. 2007.
- [17] A. Boucher, P. C. Kyriakidis, and C. Cronkite-Ratcliff, "Geostatistical solutions for super-resolution land cover mapping," *IEEE Trans. Geosci. Remote Sens.*, vol. 46, no. 1, pp. 272–283, Jan. 2008.
- [18] Q. Wang and W. Shi, "Utilizing multiple subpixel shifted images in subpixel mapping with image interpolation," *IEEE Geosci. Remote Sens. Lett.*, vol. 11, no. 4, pp. 798–802, Apr. 2013.
- [19] Q. Wang, W. Shi, and P. M. Atkinson, "Sub-pixel mapping of remote sensing images based on radial basis function interpolation," *ISPRS J. Photogramm. Remote Sens.*, vol. 92, pp. 1–15, Jun. 2014.
- [20] Y. Ge, Y. Chen, S. Li, and Y. Jiang, "Vectorial boundary-based sub-pixel mapping method for remote-sensing imagery," *Int. J. Remote Sens.*, vol. 35, no. 5, pp. 1756–1768, 2014.
- [21] Y. Ge, S. Li, and V. C. Lakhan, "Development and testing of a subpixel mapping algorithm," *IEEE Trans. Geosci. Remote Sens.*, vol. 47, no. 7, pp. 2155–2164, Jul. 2009.
- [22] H. J. Huang, J. Yu, and W. D. Sun, "Superresolution mapping using multiple dictionaries by sparse representation," *IEEE Geosci. Remote Sens. Lett.*, vol. 11, no. 12, pp. 2055–2059, Dec. 2014.
- [23] A. Villa, J. Chanussot, J. A. Benediktsson, and C. Jutten, "Spectral unmixing for the classification of hyperspectral images at a finer spatial resolution," *IEEE J. Sel. Topics Signal Process.*, vol. 5, no. 3, pp. 521–533, Jun. 2011.
- [24] F. Ling *et al.*, "Post-processing of interpolation-based super-resolution mapping with morphological filtering and fraction refilling," *Int. J. Remote Sens.*, vol. 35, no. 13, pp. 5251–5262, 2014.
- [25] Y.-F. Su, G. M. Foody, A. M. Muad, and K.-S. Cheng, "Combining pixel swapping and contouring methods to enhance super-resolution mapping," *IEEE J. Sel. Topics Appl. Earth Observ. Remote Sens.*, vol. 5, no. 5, pp. 1428–1437, Oct. 2012.
- [26] X. Xu, Y. Zhong, L. Zhang, and H. Zhang, "Sub-pixel mapping based on a map model with multiple shifted hyperspectral imagery," *IEEE J. Sel. Topics Appl. Earth Observ. Remote Sens.*, vol. 6, no. 2, pp. 580–593, Apr. 2013.
- [27] Y. Zhong, Y. Wu, X. Xu, and L. Zhang, "An adaptive subpixel mapping method based on MAP model and class determination strategy for hyperspectral remote sensing imagery," *IEEE Trans. Geosci. Remote Sens.*, vol. 53, no. 3, pp. 1411–1426, Mar. 2015.
- [28] J. M. Bioucas-Dias, A. Plaza, G. Camps-Valls, P. Scheunders, N. M. Nasrabadi, and J. Chanussot, "Hyperspectral remote sensing data analysis and future challenges," *IEEE Geosci. Remote Sens. Mag.*, vol. 1, no. 2, pp. 6–36, Jun. 2013.
- [29] M.-D. Iordache, J. Bioucas-Dias, and A. Plaza, "Sparse unmixing of hyperspectral data," *IEEE Trans. Geosci. Remote Sens.*, vol. 49, no. 6, pp. 2014–2039, Jun. 2011.
- [30] W. R. Tobler, "A computer movie simulating urban growth in the detroit region," *Econ. Geogr.*, vol. 46, pp. 234–240, Jun. 1970.
- [31] X. Li, C. Cao, and C. Chang, "The first law of geography and spatial temporal proximity," *J. Nature (China)*, vol. 29, no. 2, pp. 69–71, 2007.
- [32] *Definition of Band Sequential (BSQ) Format*. Accessed: Nov. 12, 2009. [Online]. Available: http://webhelp.esri.com/arcgisdesktop/9.3/index.cfm?topicname=BIL,_BIP,_and_BSQ_raster_files
- [33] M. K. Ng, H. Shen, E. Y. Lam, and L. Zhang, "A total variation regularization based super-resolution reconstruction algorithm for digital video," *EURASIP J. Adv. Signal Process.*, vol. 2007, Dec. 2007, Art. no. 74585.
- [34] T. Goldstein and S. Osher, "The split bregman method for L_1 -regularized problems," *SIAM J. Imag. Sci.*, vol. 2, no. 2, pp. 323–343, 2009.
- [35] X. Zhang, M. Burger, X. Bresson, and S. Osher, "Bregmanized non-local regularization for deconvolution and sparse reconstruction," *SIAM J. Imag. Sci.*, vol. 3, no. 3, pp. 253–276, 2010.
- [36] W. Yin, S. Osher, D. Goldfarb, and J. Darbon, "Bregman iterative algorithms for ℓ_1 -minimization with applications to compressed sensing," *SIAM J. Imag. Sci.*, vol. 1, no. 1, pp. 143–168, 2008.
- [37] D. C. Heinz and C.-I. Chang, "Fully constrained least squares linear spectral mixture analysis method for material quantification in hyperspectral imagery," *IEEE Trans. Geosci. Remote Sens.*, vol. 39, no. 3, pp. 529–545, Mar. 2001.
- [38] Q. McNemar, "Note on the sampling error of the difference between correlated proportions or percentages," *Psychometrika*, vol. 12, no. 2, pp. 153–157, 1947.
- [39] O. Debeir, I. Van den Steen, P. Latinne, P. Van Ham, and E. Wolff, "Textural and contextual land-cover classification using single and multiple classifier systems," *Photogramm. Eng. Remote Sens.*, vol. 68, no. 6, pp. 597–606, Jun. 2002.
- [40] Y. Zhong and L. Zhang, "An adaptive artificial immune network for supervised classification of multi-hyperspectral remote sensing imagery," *IEEE Trans. Geosci. Remote Sens.*, vol. 50, no. 3, pp. 894–909, Mar. 2012.
- [41] E. Alpaydin, *Introduction to Machine Learning*. Cambridge, MA, USA: MIT Press, Oct. 2004.
- [42] D. Schlapfer, J. Nieke, and K. I. Itten, "Spatial PSF nonuniformity effects in airborne pushbroom imaging spectrometry data," *IEEE Trans. Geosci. Remote Sens.*, vol. 45, no. 2, pp. 458–468, Feb. 2007.
- [43] R. M. Hoffer, "Computer-aided analysis of multispectral scanner data—the beginnings," in *Proc. Annu. Conf. (ASPRS)*, Mar. 2009, pp. 1–11.
- [44] D. Landgrebe, *Signal Theory Methods in Multispectral Remote Sensing*. Hoboken, NJ, USA: Wiley, 2003.



Xiong Xu (M'16) received the B.Sc. degree in photogrammetry and the Ph.D. degree in photogrammetry and remote sensing from Wuhan University, Wuhan, China, in 2008 and 2013, respectively.

He was a Post-Doctoral Researcher with Prof. A. Plaza from 2014 to 2017. He is currently an Associate Researcher with the College of Surveying and Geo-Informatics, Tongji University, Shanghai, China. His research interests include multi- and hyper-spectral image processing, deep learning in remote sensing, and remote sensing applications.



Xiaohua Tong (SM'16) received the Ph.D. degree in transportation planning and management from Tongji University, Shanghai, China, in 1999.

He was a Post-Doctoral Researcher with the State Key Laboratory of Information Engineering in Surveying, Mapping, and Remote Sensing, Wuhan University, Wuhan, China, from 2001 to 2003. He was a Research Fellow with The Hong Kong Polytechnic University, Hong Kong, in 2006, and a Visiting Scholar with the University of California at Santa Barbara, Santa Barbara, CA, USA, from 2008 to

2009. His research interests include remote sensing, GIS, uncertainty and spatial data quality, image processing for high resolution, and hyperspectral images.

Dr. Tong is the Vice-Chair of the Commission on Spatial Data Quality of the International Cartographical Association and the Co-Chair for the International Society for Photogrammetry and Remote Sensing Working Group (WG II/4) on Spatial Statistics and Uncertainty Modeling.



Antonio Plaza (F'15) received the M.Sc. and Ph.D. degrees in computer engineering from the University of Extremadura, Badajoz, Spain, in 1999 and 2002, respectively.

He is the Head of the Hyperspectral Computing Laboratory, Department of Technology of Computers and Communications, University of Extremadura. He has authored over 600 publications, including 200 journal citation report papers (145 in the IEEE journals), 23 book chapters, and 285 peer-reviewed conference proceeding papers. His research

interests include hyperspectral data processing and parallel computing of remote sensing data.

Dr. Plaza is a fellow of the IEEE for contributions to hyperspectral data processing and parallel computing of Earth observation data. He was a member of the Editorial Board of the IEEE GEOSCIENCE AND REMOTE SENSING NEWSLETTER from 2011 to 2012 and the *IEEE Geoscience and Remote Sensing Magazine* in 2013. He was also a member of the Steering Committee of the IEEE JOURNAL OF SELECTED TOPICS IN APPLIED EARTH OBSERVATIONS AND REMOTE SENSING (JSTARS). He was a recipient of the recognition of Best Reviewers of the IEEE GEOSCIENCE AND REMOTE SENSING LETTERS in 2009 and the recognition of Best Reviewers of the IEEE TRANSACTIONS ON GEOSCIENCE AND REMOTE SENSING in 2010, for which he served as an Associate Editor from 2007 to 2012. He was a recipient of the Best Column Award of the *IEEE Signal Processing Magazine* in 2015, the 2013 Best Paper Award of the JSTARS journal, and the most highly cited paper from 2005 to 2010 in the *Journal of Parallel and Distributed Computing*. He received the Best Paper Awards at the IEEE International Conference on Space Technology and the IEEE Symposium on Signal Processing and Information Technology. He served as the Director of Education Activities for the IEEE Geoscience and Remote Sensing Society (GRSS) from 2011 to 2012 and the President of the Spanish Chapter of the IEEE GRSS from 2012 to 2016. He has reviewed over 500 manuscripts for over 50 different journals. He is the former Editor-in-Chief of the IEEE TRANSACTIONS ON GEOSCIENCE AND REMOTE SENSING. He is an Associate Editor of the IEEE ACCESS. He has guest edited 10 special issues on hyperspectral remote sensing for different journals.



Jun Li (SM'16) was born in Hunan, China, in 1982. She received the Geographical Information Systems degree from Hunan Normal University, Changsha, China, in 2004, the M.Sc. degree in remote sensing and photogrammetry from Peking University, Beijing, China, in 2007, and the Ph.D. degree in electrical and computer engineering from the Instituto Superior Tecnico, Technical University of Lisbon, Lisbon, Portugal, in 2011.

From 2011 to 2012, she was a Post-Doctoral Researcher with the Department of Technology of Computers and Communications, University of Extremadura, Badajoz, Spain. He is currently a Professor with the School of Geography and Planning, Sun Yat-sen University, Guangzhou, China, where she founded her own research group on hyperspectral image analysis in 2013. She has published a total of 69 journal citation report papers, 48 conference international conference papers, and one book chapter. Her research interests include remotely sensed hyperspectral image analysis, signal processing, supervised/semisupervised learning, and active learning.

Dr. Li has been receiving several prestigious funding grants at the national and international level since 2013. Her students have also obtained important distinctions and awards at international conferences and symposia. She received a significant number of citations to her published works, with several papers distinguished as Highly Cited Papers in Thomson Reuters' Web of Science—Essential Science Indicators. She has served as a Guest Editor for a special issue in the prestigious Proceedings of the IEEE JOURNAL. She has also served as a Guest Editor for a special issue in the prestigious *International Society for Photogrammetry and Remote Sensing Journal of Photogrammetry and Remote Sensing*. She has been serving as an Associate Editor for the IEEE JOURNAL OF SELECTED TOPICS IN APPLIED EARTH OBSERVATIONS AND REMOTE SENSING since 2014.



Yanfei Zhong (M'11–SM'15) received the B.S. degree in information engineering and the Ph.D. degree in photogrammetry and remote sensing from Wuhan University, Wuhan, China, in 2002 and 2007, respectively.

He has been a Full Professor with Wuhan University since 2010. He is currently the Head of the Remote Sensing Division, State Key Laboratory of Information Engineering in Surveying, Mapping and Remote Sensing, Wuhan University. He has published over 150 research papers, including over 80 peer-reviewed articles in international journals, such as the *International Society for Photogrammetry and Remote Sensing Journal of Photogrammetry and Remote Sensing*, the IEEE TRANSACTIONS ON GEOSCIENCE AND REMOTE SENSING, the IEEE TRANSACTIONS ON IMAGE PROCESSING, and *Pattern Recognition*. His research interests include hyperspectral remote sensing information processing, high resolution remote sensing image understanding, geoscience interpretation for multi-source remote sensing data, and applications.

Dr. Zhong was a recipient of the Excellent Young Scientist Foundation selected by the National Natural Science Foundation of China, the National Excellent Doctoral Dissertation Award of China, and the 2016 Best Paper Theoretical Innovation Award from the International Society for Optics and Photonics. He was also a referee of over 30 international journals. He is serving as an Associate Editor or an Editor for the IEEE JOURNAL OF SELECTED TOPICS IN APPLIED EARTH OBSERVATIONS AND REMOTE SENSING, the *International Journal of Remote Sensing*, and *Remote Sensing*.



Huan Xie (M'14) received the B.S. degree in surveying engineering and the M.S. and Ph.D. degrees in cartography and geoinformation from Tongji University, Shanghai, China, in 2003, 2006, and 2009, respectively.

From 2007 to 2008, she was with the Institute of Photogrammetry and GeoInformation, Leibniz Universität Hannover, Hannover, Germany, funded by the China Scholarship Council, as a Visiting Scholar. Since 2009, she has been with the College of Surveying and Geo-Informatics, Tongji University, where she is currently a Professor and teaches courses related to GIS and remote sensing. Her research interests include satellite laser altimetry and hyperspectral remote sensing.

Dr. Xie has been serving as an ExCom Member of the IEEE GRSS Shanghai Chapter since 2015.



Liangpei Zhang (M'06–SM'08) received the B.S. degree in physics from Hunan Normal University, Changsha, China, in 1982, the M.S. degree in optics from the Xi'an Institute of Optics and Precision Mechanics, Chinese Academy of Sciences, Xi'an, China, in 1988, and the Ph.D. degree in photogrammetry and remote sensing from Wuhan University, Wuhan, China, in 1998.

He was a Principal Scientist for the China State Key Basic Research Project from 2011 to 2016 appointed by the Ministry of National Science and Technology of China, Beijing, to lead the Remote Sensing Program in China. He is a Chang-Jiang Scholar Chair Professor appointed by the Ministry of Education of China, Beijing, China. He has authored over 450 research papers and five books. He holds 15 patents. He has edited several conference proceedings, issues, and geoinformatics symposiums.

His research interests include hyperspectral remote sensing, high-resolution remote sensing, image processing, and artificial intelligence.

Dr. Zhang is a fellow of the Institution of Engineering and Technology. He received the 2010 Best Paper Boeing Award and the 2013 Best Paper ERDAS Award from the American Society of Photogrammetry and Remote Sensing. He regularly serves as the Co-Chair of the series International Society for Optics and Photonics conferences on multispectral image processing and pattern recognition, conference on Asia remote sensing, and many other conferences. He also serves as an Associate Editor for the *International Journal of Ambient Computing and Intelligence*, the *International Journal of Image and Graphics*, the *International Journal of Digital Multimedia Broadcasting*, the *Journal of Geospatial Information Science*, and the *Journal of Remote Sensing*, and a Guest Editor for the *Journal of Applied Remote Sensing* and the *Journal of Sensors*. He is currently serving as an Associate Editor for the IEEE TRANSACTIONS ON GEOSCIENCE AND REMOTE SENSING.